

Far Field Flow Simulation of Contra-Rotating H-Darrieus Vertical Axis Wind Turbine

B. Ko¹, S. Liu¹, Z. Fang¹, B. Nugroho^{1,a)} and R. C. Chin²

¹*Department of Mechanical Engineering, The University of Melbourne, Melbourne, Victoria, 3010, Australia*

²*School of Mechanical Engineering, The University of Adelaide, Adelaide, South Australia, 5005, Australia*

^{a)}Corresponding author: bagus.nugroho@unimelb.edu.au

Abstract. This report presents a three-dimensional Reynolds-Averaged Navier Stokes (RANS) computational fluid dynamics (CFD) investigation of Vertical Axis Wind Turbine (VAWT) with a contra-rotating arrangement. In this study, the length of the simulated domain is set to be relatively long, allowing us to investigate the wake flow generated up to 60 turbine radius (r) downstream of the model. The simulation indicates that the far field flow of the contra-rotating VAWT reaches equilibrium at approximately $40r$ downstream. Our preliminary analysis shows that at downstream distances between $20r$ to $30r$, the wake recovers between 75% – 95% of the free stream velocity, making it an ideal downstream location to place additional VAWTs. Our results also show that the contra-rotating VAWT does not generate a significant flow disturbance beyond $5r$ in the spanwise direction, suggesting that a row of spanwise arranged contra-rotating VAWTs can be separated by a short distance.

INTRODUCTION

In the last few decades due to the issue of climate change and the volatility of fossil fuel prices, there have been major shifts in the energy resource sector. More environmentally friendly and renewable energy sources such as wind energy have attracted plenty of attention, and their usage is increasing at a rapid rate around the globe [1, 2, 3]. It is estimated that by 2050 around 7% of the world's electricity will be from offshore based wind turbines [4]. That number would be significantly higher if we also consider land-based wind turbines. There are many different types of wind turbines available, in which each has its advantages and disadvantages. One type of wind turbine that has garnered popularity, particularly in regions where the wind direction is constantly changing and the wind speed is relatively low, is the Vertical Axis Wind Turbine (VAWT). This type of wind turbine is characterised by its simple overall configuration, independent of wind direction, smaller dimension and the generator is designed to be on the bottom close to the ground [5]. VAWT's unique and simple design makes it suitable for individual usage, such as on top of the houses and buildings in the urban area or small community area (i.e villages in remote areas). Recently, however, there is plenty of interest to expand the usage of VAWT in wind farms, similar to that of the HAWT [6, 7, 8, 9]. Dabiri (2011) [7] conducted a field experiment using a few pairs of 10 m tall and 1.2 m diameter VAWTs. The result shows that the power densities of VAWT can be higher than that of HAWT, by arranging VAWTs in unique layouts that allow them to extract energy from adjacent wakes. A further experiment by Kinzel et al [8] shows that the flow velocities downwind of a VAWT would return to 95% of the upwind value in just six turbine diameters downwind. Such distance is less than half of the recovery distance downwind of a typical HAWT. Hence when it is set up properly, a wind-farm that contains VAWT could be denser and produce more energy than that of HAWT. Following these experiment results, Bremseth and Duraisamy [9] conducted Computational Fluid Dynamics (CFD) simulation on a column and arrays of VAWTs. Their simulation results show that the flow interference between VAWTs would give rise to regions of excess momentum between the VAWTs, which would lead to a higher power generation.

Despite the VAWT's advantages, it is known to be less efficient than the Horizontal Axis Wind Turbine (HAWT), because only the incoming-wind faced airfoil that can generate force to rotate the motor while the rest do not. To address this problem, one could combine two or more turbines vertically to form a contra-rotating wind turbine, which would increase the amount of torque and rotation [10, 11, 12]. The challenge with the contra-rotating wind turbine is that it needs to use a specialised motor that could capture contra-rotating shaft movement [13]. Such a

motor can be difficult to build and relatively more expensive than a regular motor. Recently, however, Didane et al [10] have shown that one could design a simple VAWT, where it can run on a regular generator and without the need to use two counter-rotating shafts or contra-rotating generator (see Figure 1). The design is based on an H-Darrieus (straight bladed) wind turbine, one of the most popular and simplest forms of VAWT. The H-Darrieus wind turbine employs a simple 2D airfoil as its lift generation mechanism, which would lead to a simpler design and manufacturing process than other VAWT type wind turbines [5, 14].

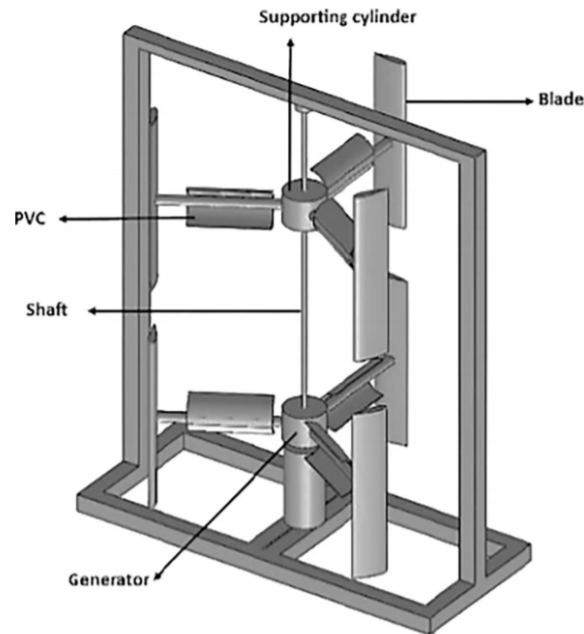


FIGURE 1: Illustration of H-Darrieus contra-rotating vertical axis wind turbine (taken from Didane et. al [11])

Looking at the potential of both H-Darrieus contra-rotating wind turbine and VAWT wind farm, it is desirable to consider the possibility of designing a wind farm of H-Darrieus contra-rotating wind turbines. One of the main challenges with designing such wind farm is to understand the turbulent wakes and far field flow behaviours downstream of the wind turbines. Such information would allow wind engineers to design an optimum wind turbine position arrangements. To the best of author's knowledge, there are limited studies in the literature that investigate the far field flow of contra-rotating VAWT. The present report focuses on the CFD simulation of H-Darrieus contra-rotating VAWT, where we will investigate its turbulent wakes. Here we will analyse its streamwise mean velocity up to 60 radii of the VAWT.

H-DARRIEUS CRWT CONFIGURATION

In this study, the turbine geometry is based on the Darrieus H-type VAWT design proposed by Didane et al. [11]. The main difference between our simulation and Didane et al. [11] model is that we do not include the additional semicircle Polyvinyl chloride (PVC) pipes to help the turbines to self-start (see Figure 2). Table 1 shows the contra-rotating VAWT configurations applied in the current study. Both upper and lower turbines are composed of three NACA0025 airfoils, where the ratio of turbine diameter, d , and chord length, c , is $d/c = 8$, and the turbine height is 500mm. The NACA0025 airfoil is chosen to closely match the NACA0021 used by Didane et al. [11]. The air properties used in the simulations are based on free stream wind velocity of $U_{in} = 12 \text{ m/s}$, $T = 25^\circ\text{C}$, where kinematic viscosity $\nu = 1.562 \times 10^{-5} \text{ m}^2/\text{s}$ and density $\rho = 1.184 \text{ kg/m}^3$. The free stream wind speed of 12 m/s is chosen to match Didane et al. [11]. The chosen wind speed is also based on the report of Nian et al. [15], where they indicate that a wind farm in Vietnam (where the geographical location is suitable for this type of VAWT) experience wind speed around 10 m/s. Therefore, 12 m/s is considered as a relatively high but frequently achievable wind speed value.

The associated revolution per minute (RPM) and tip speed ratio (TSR) are 112 *rpm* and 0.39 for the upper turbine, and 158 *rpm* and 0.55 for the lower turbine, adapted from Didane et al. [11].

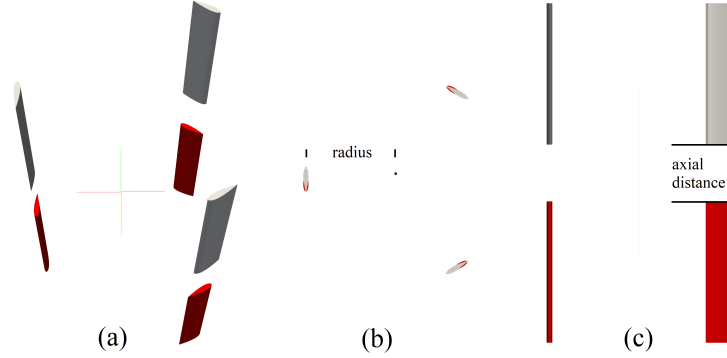
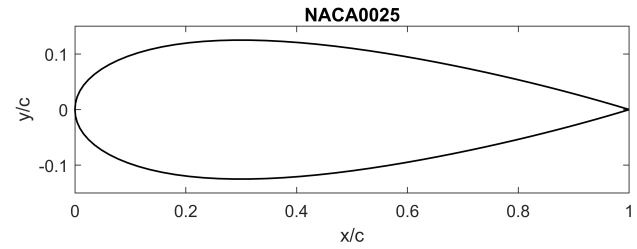


FIGURE 2: Geometric 3-dimensional configuration model of H-Darrieus contra-rotating wind turbine with (a) orthogonal (b) top and (c) front views.

TABLE 1: Model Configuration of the Contra-rotating VAWT

Configuration	Specification
Turbine Type	Darrieus VAWT
Blade Shape	Straight Blades
Cross-sectional Shape	NACA 0025
Number of Blades, n	3
Turbine Diameter, d (mm)	800
Turbine Height, h (mm)	500
Chord Length, c (mm)	100



SIMULATION SETTINGS

We conduct the Darrieus H-type contra-rotating wind turbine simulation using OpenFOAM, an open-source computational fluid dynamics (CFD) solver, on The University of Melbournes Spartan HPC (High Performing Computer) system. The flow in the simulation is considered to be unsteady, incompressible and viscous. The governing equation that is solved by the OpenFOAM is the Navier-Stokes equation which contains continuity equation:

$$\frac{\partial \bar{u}_i}{\partial x} = 0, \quad (1)$$

and the momentum equation:

$$\frac{\partial \bar{u}_i}{\partial t} + \bar{u}_j \frac{\partial \bar{u}_i}{\partial x_j} = \bar{f}_i - \frac{1}{\rho} \frac{\partial \bar{p}}{\partial x_i} + \nu \frac{\partial^2 \bar{u}_i}{\partial x_j^2} - \frac{\partial \overline{u'_i u'_j}}{\partial x_j}. \quad (2)$$

Where \bar{u}_i and u' are the time-averaged and fluctuating component of the velocity in the x_i direction, ρ is the air density, ν is kinematic viscosity, f_i represent external forces and p is the average pressure. Here we use the $k - \omega$ Shear Stress Transport (SST) as the turbulence model as it has been known to work well with H-Darrieus wind turbine [11]. The turbulent model has equations for specific turbulent kinetic energy k (m^2/s^2) and specific turbulent dissipation rate ω (s^{-1}) in the form of :

$$\frac{\partial(\rho k)}{\partial t} + \frac{\partial(pU_1 k)}{\partial x_1} = \bar{P}_k - \beta^* \rho k \omega + \frac{\partial}{\partial x_i} \left[(\mu + \sigma_k \mu_t) \frac{\partial k}{\partial x_i} \right] \quad (3)$$

$$\frac{\partial \rho \omega}{\partial t} + \frac{\partial \rho U_1 \omega}{\partial x_1} = \alpha \rho S^2 - \beta \rho \omega^2 + \frac{\partial}{\partial x_i} \left[(\mu + \sigma_\omega \mu_t) \frac{\partial \omega}{\partial x_i} \right] + 2(1 - F_1) \rho \omega^2 + \frac{1}{\omega} \frac{\partial k}{\partial x_1} \frac{\partial \omega}{\partial x_i} \quad (4)$$

Where \tilde{P}_k is the production rate of turbulent kinetic energy, F_1 is a blending function that is equal to zero away from the surface ($k - \epsilon$ model), and switches to one inside the boundary layer ($k - \omega$ model)[16].

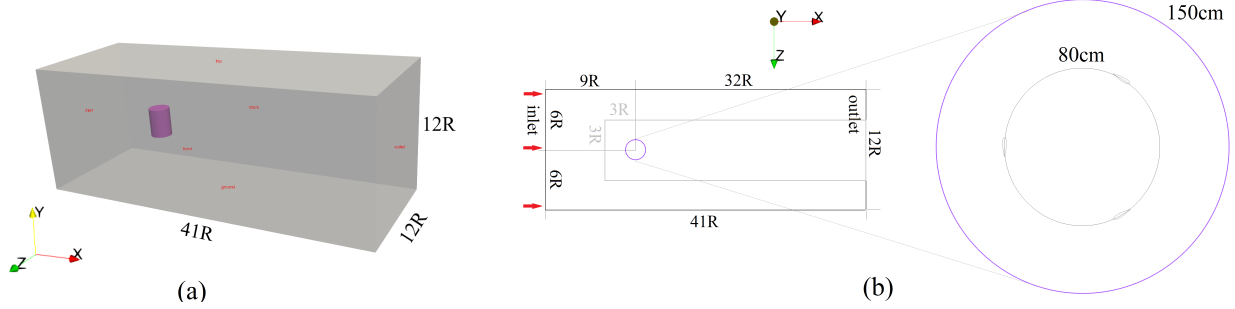


FIGURE 3: Simulation domain in (a) orthogonal view; red denotes rotating domain and dark grey denotes stationary domain, and (b) top view; light grey line denotes downstream refinement region

The computational domain consists of two parts: stationary domain and rotation domain (Figure 3(a)). The rotation domain (denoted by purple color) is further subdivided into two, the upper and the lower rotating zone, due to different rotating directions. The stationary domain is composed of six surfaces: a velocity inlet, which simulates the wind inflow along the X-axis, a pressure outlet, which simulates the atmospheric exit along the X-axis, a no-slip wall (ground) at the bottom (negative Y-direction), and three slip walls for other side surfaces. Each rotating zone has a turbine surface boundary, which is defined as a no-slip wall. The rotating domain radius R (750 mm) is defined as $1.875r$, where r is the turbine radius (400 cm), and its height H (200 cm) is defined as $4h$, where h is the turbine height (500 cm). The rotational speed is applied to cells in each rotating zone. A refinement zone is introduced to have a better resolution on the downstream far field data.

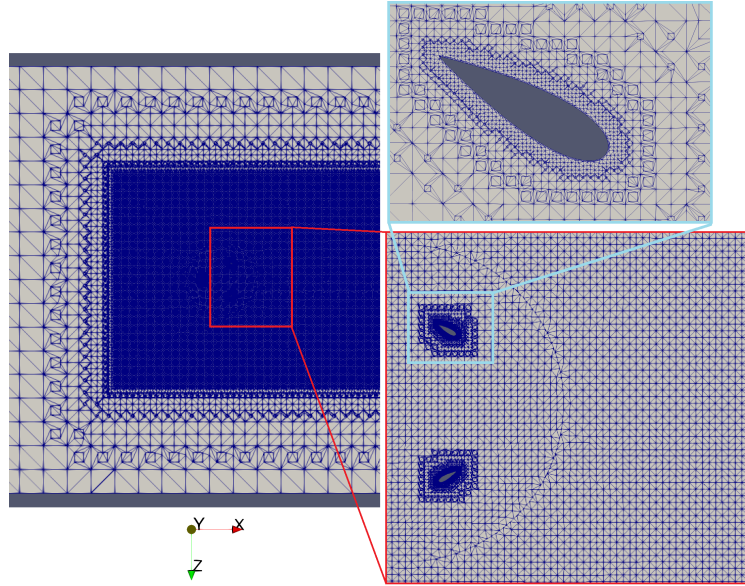


FIGURE 4: Mesh refinement near the rotating zone and the turbine

The computational domain size is $41R \times 12R \times 12R$ in the streamwise, spanwise and wall-normal direction respectively, with the refinement zone having $35R \times 6R \times 6R$, as shown in Figure 3(b). The stationary domain is discretised to achieve an average mesh resolution of $0.5 m$. The rotating domain and the refinement zone are discretised

to achieve an average mesh resolution of 0.03125 m . The grid resolution of the region around the turbine blades is further refined to an average mesh resolution of 0.0019 m . The total number of grid points for the simulation is approximately 19 Million, as shown in Figure 4. This number of grid number is chosen after a grid independence analysis, whereby the current grid resolution ensures the residuals to fall in the range of between 10^{-4} to 10^{-5} . As the grid resolution is not sufficient to resolve the boundary layer on the wind turbine blades, which is typical for RANS simulations, a wall-function is applied in the near-wall region, which is a combined function of the viscous and logarithmic laws.

RESULTS

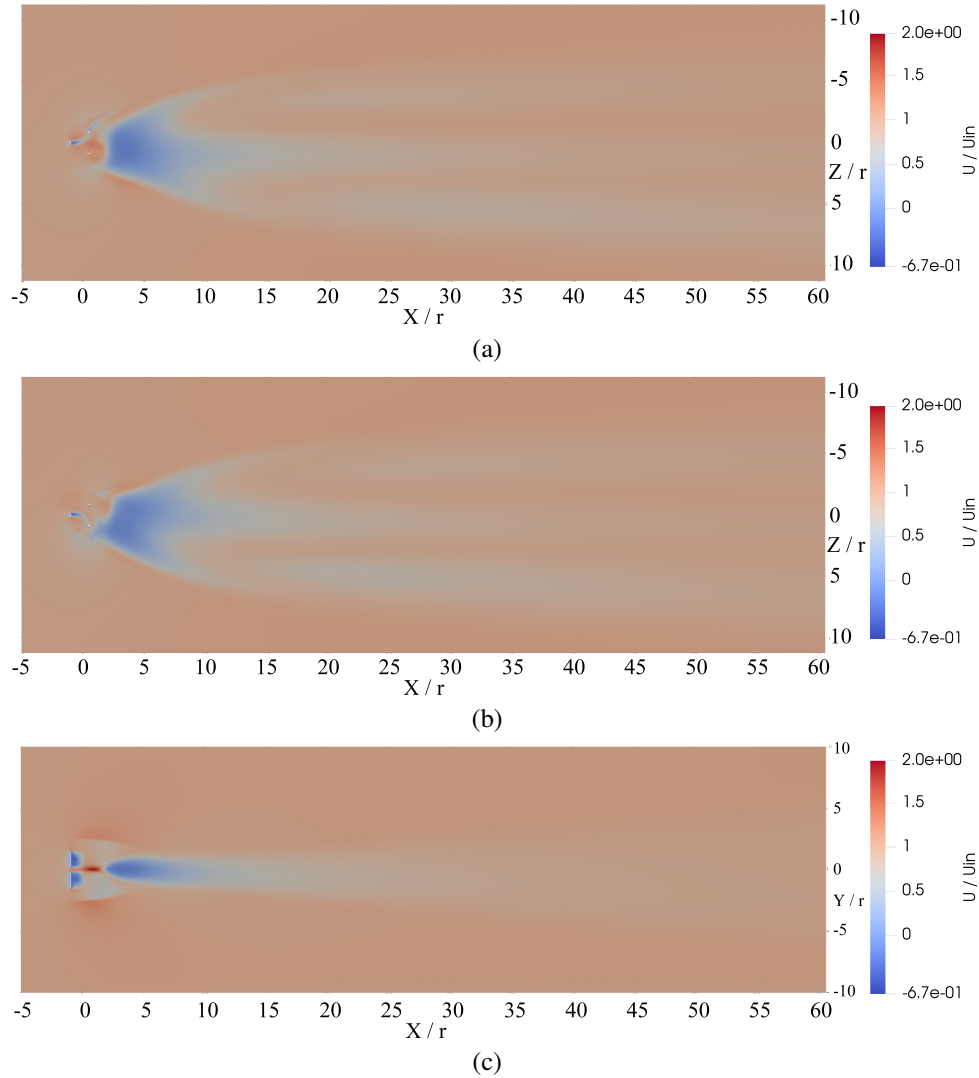


FIGURE 5: Velocity field of (a) upper turbine and (b) lower turbine in X-Z plane, and (c) side view in X-Y plane

In this section, the general results from OpenFOAM simulations and MATLAB post-processing are presented and discussed. Figure 5 shows the turbine's steady-state velocity field contour U/U_{in} , where U is mean velocity and U_{in} is the free stream velocity (red indicating a high-velocity region and blue indicates a low-velocity region). The plots are taken at three different locations, namely: the upper (Figure 5(a)) and lower turbines (Figure 5(b)), which are observed from the $X - Z$ planes at the middle of the turbines height and normal to their rotating axes; and from

the side (Figure 5(c)) which is viewed from the $X - Y$ plane at $Z = 0$, where the centre plane of both rotating axes are located. Figures 5(a) and (b) show that the flow pattern is the reverse of each other due to the different rotation directions. Both the top and the bottom turbines seem to experience a significant velocity deficit between $X/r = 2$ to 10 , where X is the streamwise distance and r is the turbine radius. A similar flow behaviour for a single-stage VAWT has been reported by Shamsoddin and Porte-Agel [17] and Akbar and Dabiri [18].

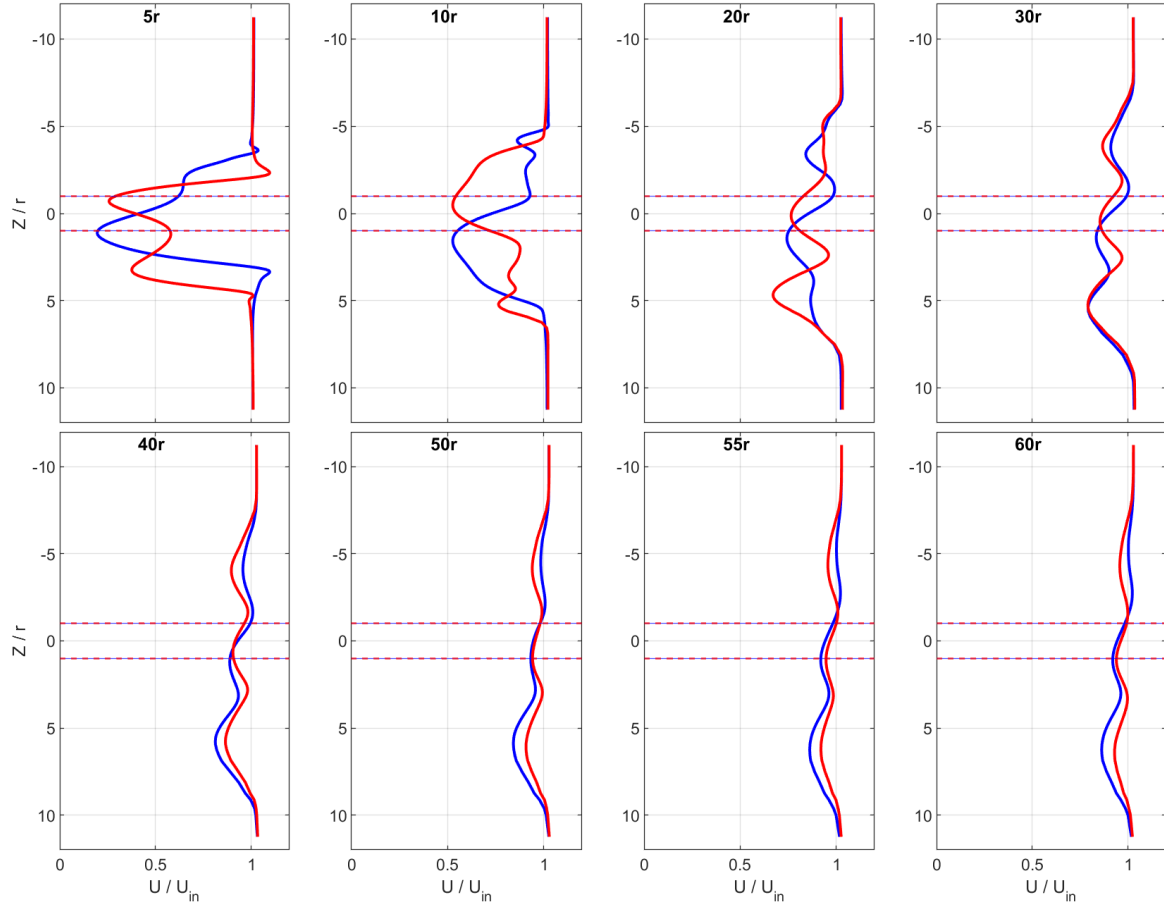


FIGURE 6: Upper (blue lines) and lower (red lines) turbine normalised mean velocities in the $X - Z$ plane (viewed from the top). The dashed blue and red lines in the $Z/r = \pm 1$ locations indicate the extension of the turbine diameter of the top and lower turbine respectively.

Figure 6 shows the span-wise profiles of the normalized streamwise velocity (viewed from the top) at different locations along the X-axis of the upper (blue) and the lower (red) turbine. The blue dashed lines in the $Z/r = \pm 1$ locations represent the extension of the turbine diameter of the top turbine, while the red dashed lines in the $Z/r = \pm 1$ locations indicate the bottom turbine. Here we are interested to look at streamwise velocity defect slices at several downstream locations, from $X = 5r$ up to $60r$. At $X = 5r$, both the top and bottom turbines experience the highest velocity defect, which is indicated by two distinct peaks at $Z/r = -1$ (for the top turbine) and $Z/r = 1$ (for the bottom turbine). Both peaks in the velocity defect profiles have an almost identical magnitude of $U/U_{in} \approx 0.2$ to 0.25 , which is quite common for VAWT [17, 18]. At this streamwise location, both turbines also show a second peak, where the top turbine is located at $Z/r \approx -2.1$ and the bottom turbine is located at $Z/r \approx 3.2$. Such a second peak has not been observed in regular VAWT. Interestingly, apart from being located further away from the centre of the radius, the secondary peak of the bottom turbine is also lower in magnitude when it is compared with the top turbine (i.e both secondary peaks have different magnitude and Z/r location). We suspect that there is a complex vortex interaction that causes such a unique phenomenon. Another possible reason is considered to be due to our simulation artefacts. Note

that these turbines are acting as motors in a fixed fluid domain rather than driven by the incoming fluid. Even though the domain is large enough, such artifacts could still occur.

From $X = 5r$ to $20r$, the velocity profile for the top and bottom turbines are the mirror image of each other (albeit asymmetric). This observation agrees with the contra-rotating configuration that the top and bottom turbines rotate clockwise and anti-clockwise respectively. At these streamwise locations, a relatively high recovery rate of wake velocity is observed for both turbines (from around 25% to 75%). Beyond those ranges, the wake from both turbines tends to spread further away from the centre and the velocity deficit dissipates with a decreasing recovery rate. The flow starts to reach equilibrium at $X = 40r$, indicated by the overlapping U/U_{in} . Despite the promising results, the asymmetric mean velocity feature of the top and bottom wind turbine at $X = 5r$ to $20r$ raises some questions. The reason for the distinction could be considered as the use of steady-state solver with RANS. Further investigation could be made by using transient solver with both RANS and LES to observe the behaviour. Despite this anomaly, figure 6 indicates that a spanwise separation of $5r$ between two contra-rotating Darrieus H-type VAWTs would be sufficient and would not disturb each other's flow significantly. A similar conclusion is also reported by Bremseth and Duraisamy [9]. The figure also indicates that ideally, we could only put a second downstream wind turbine located beyond $X = 20r$, where more than 75% of the free stream velocity is recovered.

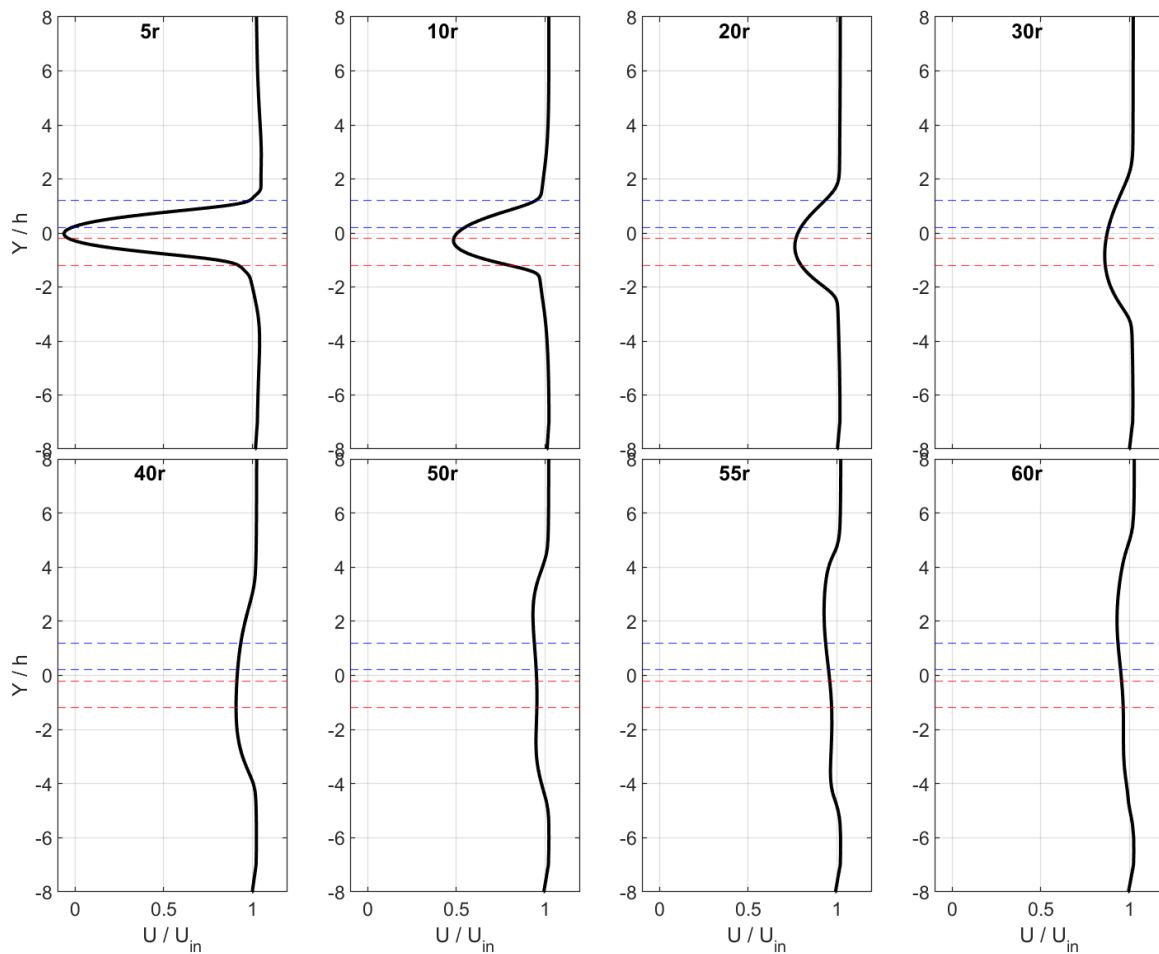


FIGURE 7: Side view of normalised mean velocities in the $X - Y$ plane (viewed from the side).

To better understand the overall flow behaviour of the VWAT, we analyse the flow field from the side view ($X - Y$ plane), and to see the evolution in the streamwise velocity U over the wall-normal (vertical) direction. The side view of the streamwise velocity profile is shown in Figure 7, here the blue dashed lines and the red dashed lines represent

the height of the upper turbine and the lower turbine respectively. The plot indicates that at $X = 5r$ the velocity defect is very high, particularly at the midsection between the top and bottom turbine. As we move downstream, the flow experience a relatively fast recovery up to $X = 20r$, beyond this location the recovery rate decreases and reaches equilibrium around $X = 40r$ (where 90% of the free stream velocity is recovered). When we look at the streamwise location $X = 10r$, the midsection of the top and bottom turbines (i.e at $Y/h = 1$ and -1) has recovered around 90% of the free stream velocity. This indicates that having a second contra-rotating Darrieus H-type VAWT located at $X = 10r$ downstream of the first wind turbine is acceptable. The result is comparable with the finding of Kinzel et al [8] where the flow velocities return to 95% of the upwind value within six turbine diameters (or $12r$). Note, however, that the $X = 10r$ is based on the streamwise velocities over a wall-normal (vertical) locations, when it is based on span-wise (horizontal) locations we have previously shown that the VAWT should be located at $X = 20r$ or beyond. It is quite difficult to determine the exact streamwise location of the second turbine without conducting a more accurate and expensive simulation such as LES. This includes looking at other parameters such as type of airfoil, the lateral distance between the top and bottom turbine, etc. Beyond this, it is also desirable to conduct simulation with more than one contra-rotating Darrieus H-type VAWT.

CONCLUSION

In this study, a Reynolds-Averaged Navier Stokes (RANS) CFD steady-state simulation is conducted on a Darrieus H-type contra-rotating vertical axis wind turbine. We analysed the mean streamwise velocity both on the $X - Y$ and $X - Z$ planes between $X/r = 5$ up to 60. The results show that the flow in the far field reaches equilibrium at $X/r \approx 40$. Our preliminary analysis also suggests that a row of Darrieus H-type contra-rotating VAWT, arranged in spanwise would only need a separation distance of around $5r$. Such distance is sufficient in preventing flow disturbance from the adjacent wind turbine. With regards to streamwise separation distances between the upstream and downstream VAWTs, our analysis suggests hows that the separation distances should be between $X = 20r$ to $30r$. At these distances, the downstream VAWT will be able to capture 75% – 95% of the free stream velocity.

ACKNOWLEDGMENTS

This research was undertaken using the LIEF HPC-GPGPU Facility hosted at the University of Melbourne. This Facility was established with the assistance of LIEF Grant LE170100200.

REFERENCES

- [1] G. Joselin Herbert, S. Iniyan, E. Sreevalsan, and S. Rajapandian, *Renewable and Sustainable Energy Reviews* **11**, 1117 – 1145 (2007).
- [2] D. Y. C. Leung and Y. Yang, *Renewable and Sustainable Energy Reviews* **16**, 1031 – 1039 (2012).
- [3] Y. Kumar, J. Ringenberg, S. S. Depuru, V. K. Devabhaktuni, J. W. Lee, E. Nikolaidis, B. Andersen, and A. Afjeh, *Renewable and Sustainable Energy Reviews* **53**, 209 – 224 (2016).
- [4] M. Esteban and D. Leary, *Applied Energy* **90**, 128 – 136 (2012).
- [5] M. M. Aslam Bhutta, N. Hayat, A. U. Farooq, Z. Ali, S. R. Jamil, and Z. Hussain, *Renewable and Sustainable Energy Reviews* **16**, 1926 – 1939 (2012).
- [6] W. Tjiu, T. Marnoto, S. Mat, M. H. Ruslan, and K. Sopian, *Renewable Energy* **75**, 50 – 67 (2015).
- [7] J. O. Dabiri, *Journal of Renewable and Sustainable Energy* **3**, p. 043104 (2011).
- [8] M. Kinzel, Q. Mulligan, and J. O. Dabiri, *Journal of Turbulence* **13**, p. N38 (2012).
- [9] J. Bremseth and K. Duraisamy, *Theoretical and Computational Fluid Dynamics* **30**, 387–401 (2016).
- [10] D. H. Didane, N. Rosly, M. F. Zulkafli, and S. S. Shamsudin, *Renewable Energy* **115**, 353–361 (2018).
- [11] D. H. Didane, N. Rosly, M. F. Zulkafli, and S. S. Shamsudin, *Sustainable Energy Technologies and Assessments* **31**, 43–53 (2019).
- [12] B. Ko, S. Liu, F. Zhou, Y. Ahmudiarto, B. Naguroho, and C. Chin, “Numerical simulation of two-stages contra-rotating vertical axis wind turbine,” (2020).
- [13] J. Booker, P. Mellor, R. Wrobel, and D. Drury, *Renewable Energy* **35**, 2027 – 2033 (2010).
- [14] A. Bianchini, G. Ferrara, and L. Ferrari, *Energy Conversion and Management* **89**, 690 – 707 (2015).
- [15] V. Nian, Y. Liu, and S. Zhong, *Applied Energy* **233-234**, 1003–1014 (2019).

- [16] F. R. Menter, M. Kuntz, and R. Langtry, *Turbulence, heat and mass transfer* **4**(1), 625–632 (2003).
- [17] S. Shamsoddin and F. Porte-Agel, *Energies* **6**, 366.1–23 (2016).
- [18] M. Abkar and J. O. Dabiri, *Journal of Turbulence* **18**, 373–389 (2017).
- [19] J. O. Dabiri, *Journal of Renewable and Sustainable Energy* **3**, 043104.1–12 (2011).